

# Face-selective electrostatic control of hydrothermal zinc oxide nanowire synthesis

Jaebum Joo<sup>1,2\*</sup>, Brian Y. Chow<sup>1,3\*</sup>†, Manu Prakash<sup>1,4</sup>†, Edward S. Boyden<sup>1,3</sup> and Joseph M. Jacobson<sup>1</sup>

**Rational control over the morphology and the functional properties of inorganic nanostructures has been a long-standing goal in the development of bottom-up device fabrication processes. We report that the geometry of hydrothermally grown zinc oxide nanowires<sup>1–4</sup> can be tuned from platelets to needles, covering more than three orders of magnitude in aspect ratio (~0.1–100). We introduce a classical thermodynamics-based model to explain the underlying growth inhibition mechanism by means of the competitive and face-selective electrostatic adsorption of non-zinc complex ions at alkaline conditions. The performance of these nanowires rivals that of vapour-phase-grown nanostructures<sup>5,6</sup>, and their low-temperature synthesis (<60 °C) is favourable to the integration and *in situ* fabrication of complex and polymer-supported devices<sup>7–9</sup>. We illustrate this capability by fabricating an all-inorganic light-emitting diode in a polymeric microfluidic manifold. Our findings indicate that electrostatic interactions in aqueous crystal growth may be systematically manipulated to synthesize nanostructures and devices with enhanced structural control.**

As a low-temperature aqueous process, hydrothermal synthesis<sup>1–3,10–12</sup> or crystallization from supersaturated aqueous solutions<sup>3,10</sup> holds great promise for nanostructure synthesis on a variety of substrates, and so far has been reported in the construction of several energy-harvesting and electronic devices<sup>13,14</sup>. The functions of these devices are critically linked to nanostructure morphology and hence require parameter tuning for optimal performance. Therefore, a predictive model-based hydrothermal synthesis that enables rational control over nanostructure morphology would greatly advance bottom-up nanoscience. To this end, many growth parameters have been previously explored to manipulate the morphology of hydrothermally synthesized ZnO nanowires<sup>3,10</sup>, including the addition of auxiliary agents such as organic ligands and metal-ion impurities<sup>2,4,12,14,15</sup>. Previous findings that pH-dependent electrostatic interactions between zinc reactants and the crystal can influence the preferred growth direction<sup>2,11,16,17</sup> suggest that such interactions may provide a potential modality of control over ZnO nanowire morphology. Expanding on these explorations, a rational approach to systematically alter nanowire morphology bidirectionally (namely increasing or decreasing the aspect ratio) by means of electrostatics is developed here.

The primary principle underlying rational control during hydrothermal synthesis is face-selective electrostatic interaction. By introducing ancillary non-zinc sulphates into this reaction, we are able to systematically control the local reaction environment during the growth phase. The non-zinc ions form charged but

largely unreactive complexes that can localize to the oppositely charged crystal surfaces, thereby competitively limiting the access of the reactive zinc intermediates and inhibiting growth in a crystal face-specific manner (Fig. 1). This mechanism is supported by the classical thermodynamic modelling provided here and validated by the ability to predict the effect of introducing various non-zinc ions on the aspect ratio of ZnO nanowires. The further understanding of electrostatics in controlled aqueous growth may enhance the syntheses of other inorganic structures, such as biomineralized and biomimetically crystallized nanostructures<sup>18,19</sup>, or *in situ* grown layer-by-layer assemblies<sup>20</sup>.

Single-crystalline nanowires were grown on substrates with zinc oxide seed layers in aqueous solutions of 10 mM zinc sulphate with 0.3 M ammonium chloride to improve zinc-ion solubility (pH = 11, 60 °C). These reagents and the alkaline reaction condition were chosen because speciation plots of the relative concentrations of intermediate metal hydroxide- and amine-complexes could be calculated from known constants (see Supplementary Figs S1–S3 for parametric optimization for specific conditions). These plots are shown in Fig. 2a,b for individual zinc complex ions and their intermediates, binned by charge, respectively (see Supplementary Fig. S2 for constants and supersaturation plots). At pH = 11, both positive and negative complex ions are present, and thus each species may interact with the crystal in a face-selective manner<sup>2,11,16,17</sup>, because the negative (0002) top surface plane and positive (10 $\bar{1}$ 0) sidewalls were found to be differentially charged (as measured by atomic force microscopy (Supplementary Fig. S6) and X-ray photoelectron spectroscopy (Supplementary Fig. S7)).

Whereas adjusting pH alone in a zinc-only system had modest impact on aspect ratio (<1.5-fold range; Supplementary Fig. S5), adding charged non-zinc complex ions induces pronounced changes in aspect ratio (Fig. 1a,b) by a face-selective crystal growth inhibition mechanism that could be leveraged to systematically control aspect ratio over a >1,000-fold range. For example, introducing a small amount of cadmium sulphate into the reaction mixture (<20% equivalent versus zinc) led to low aspect ratio platelets (0.1 height/diameter ratio), suggesting that the positively charged cadmium complexes (>99% positive at pH = 11, Fig. 2c) were electrostatically attracted to the negatively charged top (0002) face, thus inhibiting growth along the preferred *c* axis by limiting the access of Zn complexes. Conversely, introducing aluminium sulphate into the reaction had the opposite effect, leading to high aspect ratio structures (>100 height/diameter ratio) by the suppression of sidewall growth from the negatively charged Al complexes (Fig. 2d).

<sup>1</sup>Center for Bits and Atoms, The Media Laboratory, Massachusetts Institute of Technology, Cambridge, Massachusetts 02139, USA, <sup>2</sup>Department of Materials Science and Engineering, Massachusetts Institute of Technology, Cambridge, Massachusetts 02139, USA, <sup>3</sup>Department of Biological Engineering and Department of Brain and Cognitive Sciences, Massachusetts Institute of Technology, Cambridge, Massachusetts 02139, USA, <sup>4</sup>Harvard Society of Fellows, Harvard University, Cambridge, Massachusetts 02138, USA. †Present addresses: Department of Bioengineering, University of Pennsylvania, Philadelphia, Philadelphia 19104, USA (B.Y.C.); Department of Bioengineering, Stanford University, Stanford, California 94305, USA (M.P.).

\*e-mail: jbjoo@alum.mit.edu; bchow@media.mit.edu.

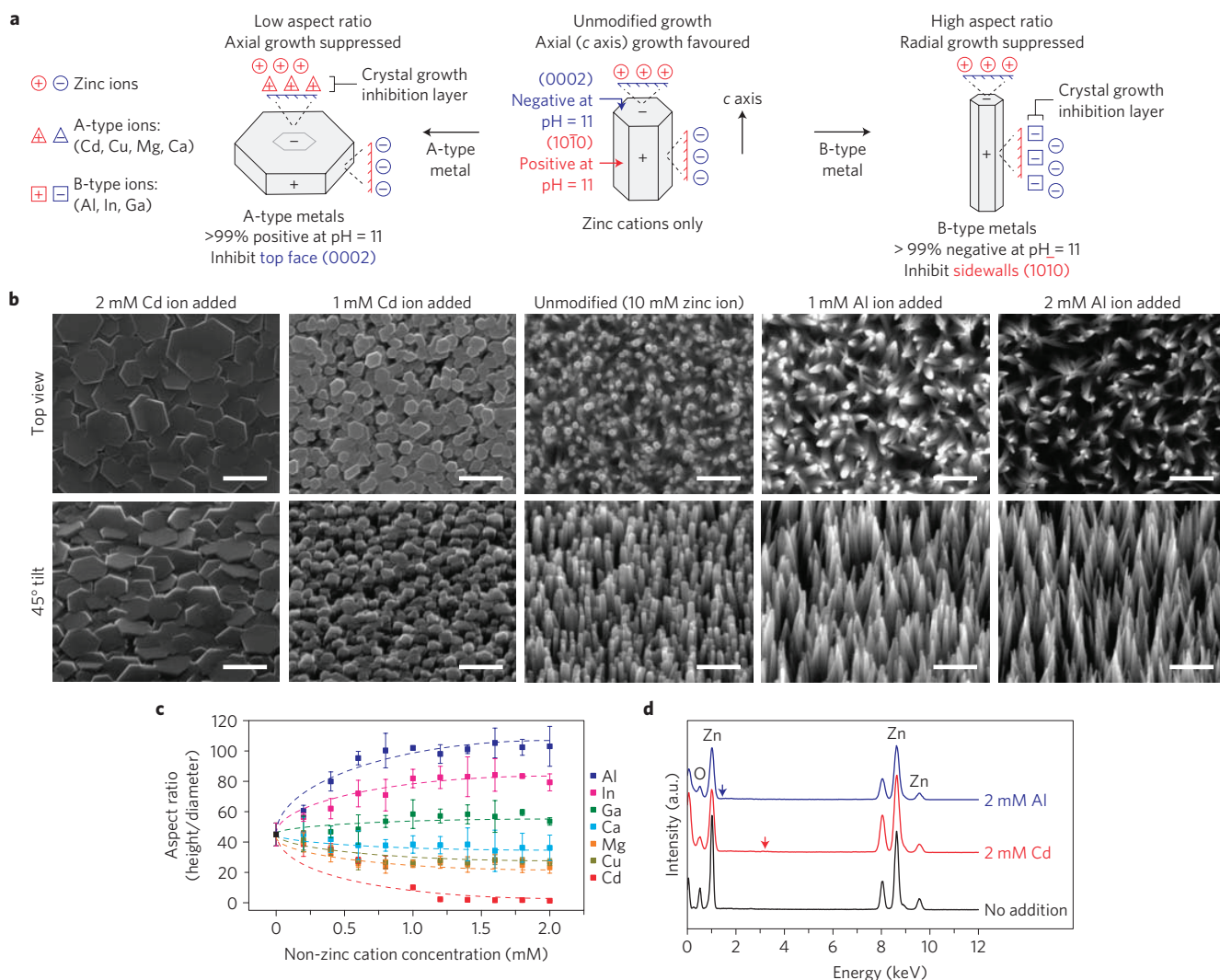


**Figure 1 | Rational control over zinc oxide nanowire morphology by means of face-selective electrostatic crystal growth inhibition.** **a**, Mechanism of control by non-zinc metal sulphates in the bath solution. A-type cations (positive at pH 11; Cd, Cu, Mg, and Ca) suppress axial growth at the negative (0002) face by limiting zinc complex-ion access, thus promoting platelet formation. Similar interactions between B-type ions (negative at pH 11; Al, In, Ga) lead to high aspect ratio nanowires grown in the presence of Cd or Al. Scale bars = 500 nm. **b**, Scanning electron micrographs of ZnO nanowires grown in the presence of Cd or Al. Scale bars = 500 nm. **c**, The aspect ratio was tunable over a >1,000-fold range (data point and error bars correspond to mean  $\pm$  one standard deviation). Dotted trend lines are to guide the eye. **d**, Energy dispersive X-ray spectra of nanowires grown in the presence of 2 mM Al or Cd do not show readily observable Al (blue arrow, 1.49 keV) or Cd (red arrow, 3.13 keV) peaks.

Ancillary metal sulphates that formed predominately positively charged complex ions at pH = 11 were categorized as A-type (Cd, Cu, Mg, Ca), whereas ions that formed predominately negatively charged complexes were categorized as B-type (Al, In, Ga). The correlations between the aspect ratio and the relative charge distribution of complex ions, in which A-type and B-type ions promote low and high aspect ratio growth, respectively, were consistent for all sulphates tested (Fig. 1c and Supplementary Fig. S8), thus further supporting the model of face-selective electrostatic crystal growth inhibition (the presence of both metal ions was accounted for in all co-speciation plots, but typically led to <1% change in distributions). It is important to note that the tapered needle- or obelisk-like ends of high-aspect-ratio nanowires (resulting from the addition of B-type metals) were formed by multiple steps of hexagonal layers of growth with decreasing surface area<sup>21</sup>, consistent with expected layer-by-layer growth mechanisms<sup>21,22</sup> (Supplementary Fig. S9). The taper does not represent the (10 $\bar{1}$ 1) facets that are otherwise at 60° to the (0002) plane<sup>23</sup>. It should also be noted that factors beyond

electrostatics may play a role, particularly at neutral pH, highly elevated temperature and/or extremely long reaction times (see Supplementary Information and Fig. S13). However, under the conditions reported here, the mechanism of bidirectional control over nanowire aspect ratio was dominated by electrostatics.

Given the low temperature, it was anticipated that non-zinc ions would have low incorporation rates into the growing ZnO crystal and, instead, their presence would primarily lead to crystal growth inhibition. Importantly, ZnO nanowires hydrothermally grown in the presence of non-zinc ions (2 mM, 20% equivalent versus zinc) did not seem to be significantly altered in their primary structure or optical properties, as confirmed by X-ray diffraction (Supplementary Fig. S10) and photoluminescence measurements ( $\lambda = 378$  nm band-edge emission) (Supplementary Fig. S11). The energy-dispersive X-ray spectroscopy (EDS) plots for ZnO nanowires grown in the presence of cadmium or aluminium lack a readily observable 3.13 keV Cd peak or 1.49 keV Al peak (red and blue arrows in Fig. 1d, respectively). The findings above were consistent for all other ions tested. The limited

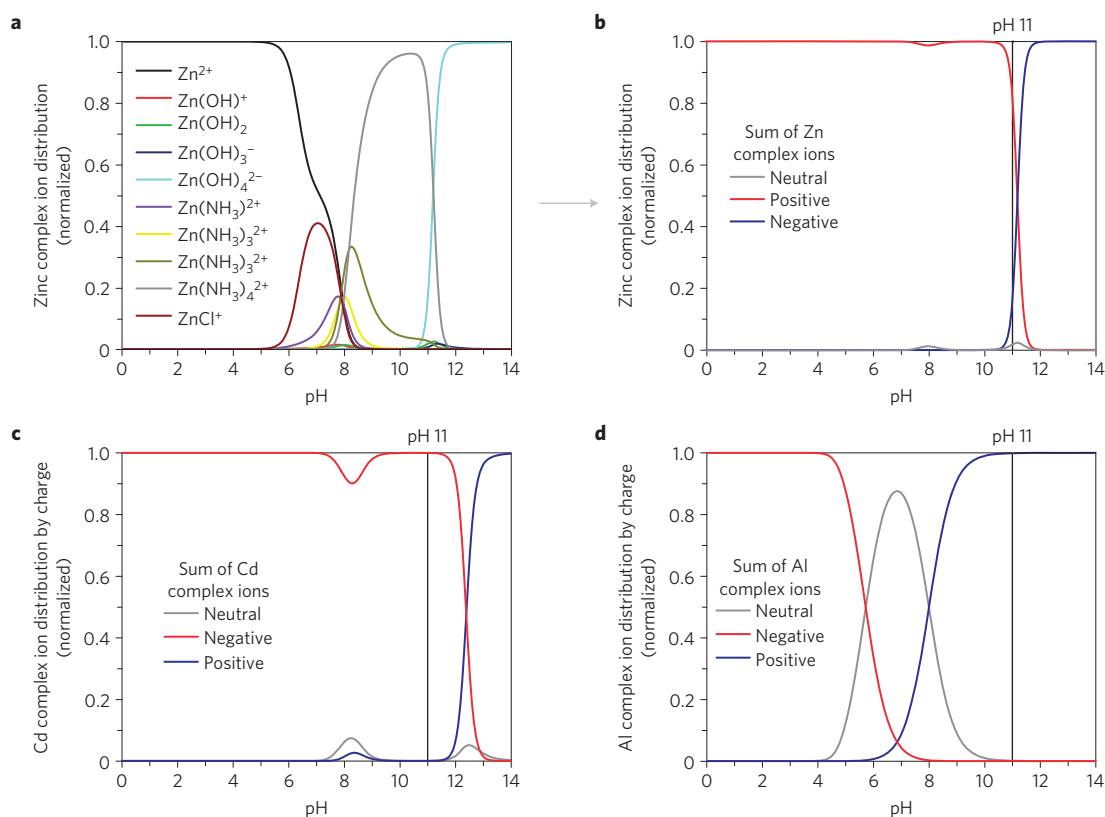


**Figure 2 | Thermodynamic modelling of electrostatic interactions during hydrothermal synthesis.** Relative concentrations of complex ion products formed from hydrolysis and aminolysis of metal sulphates were calculated from known reaction constants to derive pH-dependent speciation plots. **a,b**, Zinc complex ion distribution in a solution of 10 mM ZnSO<sub>4</sub> and 0.3 M NH<sub>4</sub>Cl, normalized to the sum of the total ions, for individual species (**a**) and binned by charge (**b**). **c,d**, Speciation plots for Cd (**c**) and Al (**d**) complex ions binned by charge (also with 0.3 M NH<sub>4</sub>Cl), as exemplar A- and B-type ions (see Fig. 1). Cd or Al complex ions are >99% positively or negatively charged at pH = 11, respectively. The model predicts face-selective crystal growth inhibition through the electrostatic adsorption of positive Cd complex ions at the negative (0002) plane, or of negative Al complex ions at the positive (10 $\bar{1}0$ ) plane.

incorporation or alteration of intrinsic material properties during the low-temperature aqueous synthesis differs from the more significant ion exchange or doping that occurs for high-temperature aqueous reactions driven in pressurized autoclaves<sup>2,24</sup>, at high temperature in organic solvents<sup>25</sup> or during co-introduction of gases in vapour–liquid solid (VLS) synthesis<sup>6</sup>.

As a result of the large formation enthalpy required for non-zinc ions to be incorporated into the ZnO crystal, the estimated maximum solubility or doping achievable under the conditions here is  $\sim 10^{-5}$  (see Supplementary Information). Given this low solubility, the electrostatically adsorbed ancillary complexes mainly blocked the available crystal surface sites to inhibit Zn-complex binding. However, limited incorporation is expected on the basis of the estimated solubility and modest increase/decrease in defect emission (Supplementary Fig. S11), and the doping is more readily observed at much higher temperature and pressure<sup>2,24</sup> (for example, increased estimated maximum solubility by  $\sim 10^2$  at 300 °C and  $> 10^8$  Pa). Thus, the ability to use inorganic ions largely as surface-binding ligand-like complexes highlights the importance of maintaining low synthesis temperatures for morphology control.

The material compatibility and potential low-cost nature (including resource consumption) of the low-temperature aqueous synthesis were underlying motivations for developing systematic control mechanisms towards the enhancement of geometry-coupled properties and manufacturing of polymer-supported devices. Accordingly, we demonstrate greatly improved field emission from ZnO nanowires formed in the presence of aluminium ions, then create polymer-supported flexible a.c.

electroluminescent devices with improved luminance efficiency, and construct a multilayer optoelectronic device completely *in situ* within a polymeric microreactor.

As the field emission of a nanoneedle scales as  $\sim d/r$  (where  $d$  is nanowire length and  $r$  is the apex radius) accelerating to the Fowler–Nordheim equations<sup>26</sup>, we exploit the above synthesized nanostructures as a field-emission source. Field emission of ZnO nanowires was greatly enhanced by the addition of aluminium sulphate into the growth solution (Fig. 3a), with turn-on field values (to reach  $10 \mu\text{A cm}^{-2}$ ) improved by a factor of  $> 8$  over nanowire emitters grown under unmodified conditions ( $0.45 \text{ V } \mu\text{m}^{-1}$  with 2 mM Al versus  $3.70 \text{ V } \mu\text{m}^{-1}$  without). Conversely, field emission was inhibited by the addition of cadmium. The calculated field enhancement factor  $\beta = 2.83 \times 10^4$  for nanowires grown in the presence of 2 mM aluminium sulphate (aspect ratio = 103) versus  $\beta = 2.08 \times 10^3$  without modifiers was a near 14-fold improvement (Supplementary Fig. S14). These values for turn-on and enhancement rival those reported for VLS-synthesized carbon nanotube emitters (turn-on  $\sim 0.8 \text{ V } \mu\text{m}^{-1}$ ,  $\beta = 1,000\text{--}35,000$ ; ref. 27), despite the very low temperature synthesis ( $< 60$  °C) that is favourable to device integration and *in situ* fabrication of polymer-supported nanodevices.

The combination of low-temperature processing in an aqueous environment and enhanced field emission is ideal for the fabrication of polymer-based, nanowire-embedded a.c. electroluminescent devices (NW-ACEL) (Fig. 3b–e). In a typical ACEL device, accelerated electrons from the emitter excite dopant atoms in a phosphor, leading to photon emission on atom relaxation to the

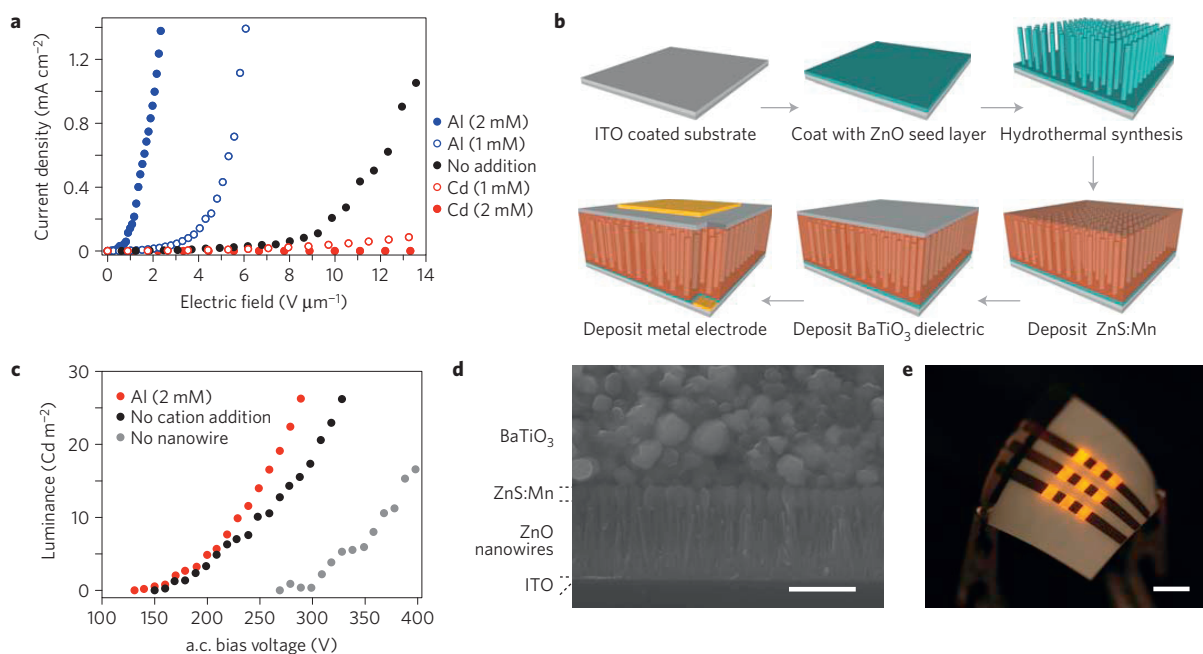


**Figure 3 | Morphology-coupled field emission of ZnO nanowires for nanowire-embedded a.c. electroluminescent devices (NW-ACEL).** **a**, Field emission of nanowires grown in the presence of Al (blue), no additional non-zinc ions (black), or Cd (red). Nanoneedles formed in the presence of 2 mM aluminium sulphate had similar emissivity to single-walled carbon nanotubes, despite the low-temperature synthesis ( $<60^\circ\text{C}$ ). **b**, Process flow for a NW-ACEL device, where ZnO nanowires enhance field emission to the phosphor from the dielectric. **c**, The luminance and efficiency (Supplementary Table S2) of the ACEL device are improved by incorporating the NW-field enhancement layer (black), particularly by high aspect ratio nanoneedles (red). **d**, Cross-sectional scanning electron micrographs of the device. Scale bar =  $1\ \mu\text{m}$ . **e**, NW-ACEL device fabricated on flexible polyethylene terephthalate (PET). The device was operated at  $260\ \text{V}_{\text{rms}}$  at 5 kHz. Scale bar = 5 mm.

ground state. ACEL devices typically have poor efficiency, and thus to improve performance, a NW-ACEL device—with nanoneedles embedded into a ZnS:Mn phosphor layer to enhance field emission from the dielectric ZnO seed layer—was fabricated on flexible, metal-coated polyethylene terephthalate (PET). The yellow/orange electroluminescence spectrum matched the photoluminescence spectrum of the phosphor (Supplementary Fig. S15), indicating that the nanoneedles acted as a field-enhancement layer, as opposed to directly emitting by electron–hole recombination within the semiconductor. The voltage-dependent luminance curves (Fig. 3c) show that the enhancement layer lowers the turn-on voltage by a factor of typically 1.5–2 per luminance unit, and improves maximum luminance efficiency by an order of magnitude (Supplementary Table S2).

Furthermore, polymer-compatible low-temperature *in situ* syntheses give possibilities beyond integration onto plastics, such as synthesis in elastomeric microfluidic environments<sup>7,28</sup>. When nanowires were synthesized in a continuous flow polydimethylsiloxane microreactor, the addition of cadmium and aluminium ions had the same effect on morphology change as in the batch synthesis process (Supplementary Figs S16 and S17). Synthesis rates were five times higher in the microfluidic device than in bulk solution because of the constant replenishing of reagents and clearance of homogenous nucleants that consume reactants in solution. Aspect ratios of the structures were effectively unchanged by growth in the microfluidic environment, which supports the notion of improved mass transport being dominant. The nanowire vertical growth rate in the microfluidic device was typically  $1.5\text{--}2\ \mu\text{m}\ \text{h}^{-1}$  versus  $0.3\text{--}0.4\ \mu\text{m}\ \text{h}^{-1}$  in the optimized batch reactor.

Beyond improved mass transport, hydrothermal synthesis in a microfluidic environment enables parallel screening of synthesis parameters with minimal reagent consumption (Supplementary Fig. S17). Microfluidics-based, surface-adherent synthesis also offers a route towards simultaneous spatial patterning of functional

materials<sup>9,29,30</sup>. As an example, we demonstrate an all-inorganic *in situ* fabricated multi-layer light-emitting diode, by sequentially flowing solution-processable reagents (Fig. 4). Here, the microfluidic manifold acts not only as a micro-reactor that improves the control over synthesis parameters and vastly diminishes reagent consumption, but also as the bottom-up fabrication house of a multilayer opto-electronic device, and finally, as the packaged end-device itself. The self-aligned *in situ* synthesis and integration into a functional device eliminates the transfer printing or etching steps typically involved in flexible electronics.

The metal–insulator–semiconductor light emitting diode (M–I–S LED) was *in situ* fabricated by sequentially synthesizing nanowires in a microfluidic manifold on top of indium tin oxide (ITO)-coated glass or PET, and subsequently flowing in an insulating spin-on-glass through the channel, followed by a low-melting solder that fills the remainder of the channel<sup>8</sup> (Fig. 4a,b). The device had an apparent 4 V turn-on voltage and a  $10^{-8}\ \text{A}$  reverse current (or  $5 \times 10^{-6}\ \text{A}\ \text{cm}^{-2}$  current density, Supplementary Fig. S18), both indicative of diode function. The fully fabricated and packaged device is optically transparent, as shown in the top inset of Fig. 4c, and light emission from an individually addressed pixel in the ON and OFF states is shown in the lower insets (Fig. 4c). The ability to completely *in situ* fabricate a multi-layer all-inorganic device with minimal reagent consumption highlights the importance of low-temperature hydrothermal synthesis and improved mechanisms for systematic control.

The chemical system presented here provides a framework for an understanding of pH-dependent surface interactions in complex reaction mixtures, on which one can build further understanding. Our model-based experiments established electrostatics as a dominant control mechanism in low-temperature alkaline hydrothermal synthesis, and further demonstrated the efficient creation of ZnO nanowire-based devices with enhanced properties and critical features for manufacturing nanostructure-based devices

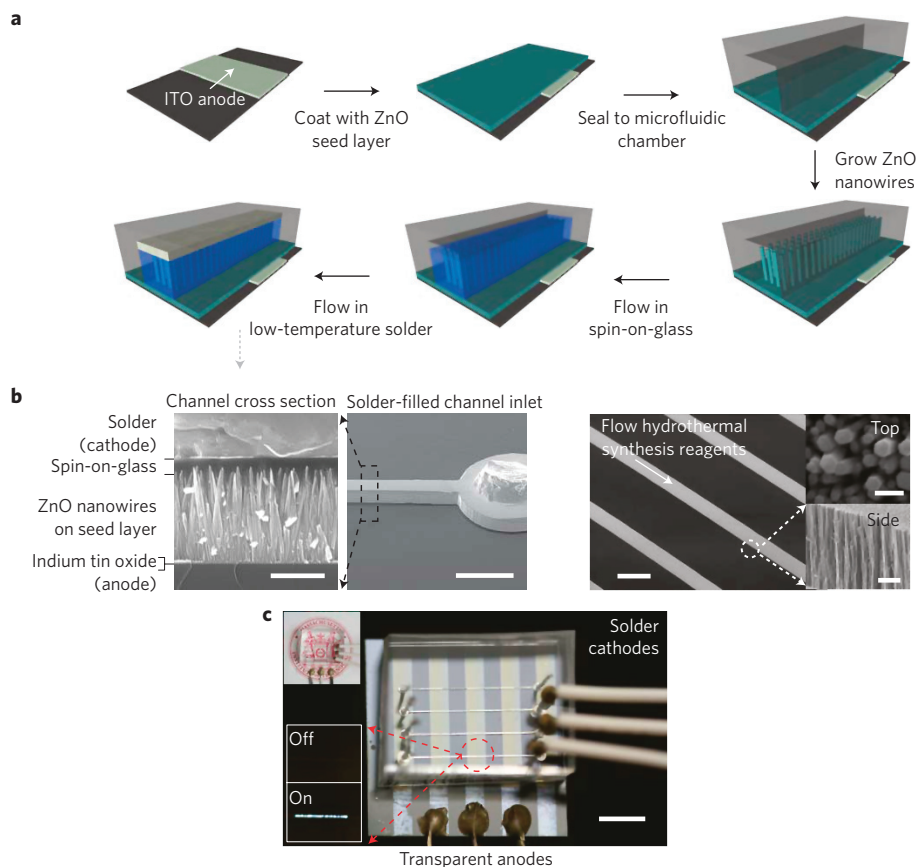


**Figure 4 | *In situ* fabrication of an all-inorganic multi-layer opto-electronic device in a microfluidic manifold. a**, Process flow for the *in situ* fabrication of a metal-insulator-semiconductor light-emitting diode (M-I-S LED). The polymeric manifold serves as a micro-reactor, bottom-up fabrication house, and the packaged end-device itself. **b**, Scanning electron microscopy characterization of the device. Left panels: Cross-section of the complete device. Scale bars = 500 nm (left), 500  $\mu\text{m}$  (right). Right panels: Nanowires grown in the microfluidic environment exhibit conformal sidewalls and a fivefold increased growth rate (over batch synthesis). Scale bars = 200  $\mu\text{m}$  (left), 500  $\mu\text{m}$  (top right), 2  $\mu\text{m}$  (bottom right). **c**, Transparent M-I-S LED imaged at a slight angle to enhance feature contrast. Top inset depicts transparency of the device at a perpendicular view point. Bottom inset shows emission in the on- and off-states at a forward bias of 10 V. Scale bar = 5 mm.

with respect to cost, material integration compatibility, and resource consumption. The synthesis is amenable to processing in microfluidic reactors, yielding multi-layer *in situ* synthesis paradigms for spatially complex functional devices. Thus, the development of an electrostatic mechanism to systematically manipulate nanowire aspect ratio may further nanomaterials synthesis chemistry towards the goal of rational control over nanostructure morphology.

## Methods

Single-crystalline nanowires were grown on substrates with zinc oxide seed layers (deposited by sputtering or spin-coating of sol-gels), in aqueous solutions of 10 mM zinc sulphate and 0.3 M ammonium chloride at pH = 11, 50–60 °C. Non-zinc metal sulphates were added to the solution before growth. All reagents were used as received from Sigma-Aldrich unless noted otherwise; deionized water was 18.2 M $\Omega$  Millipore water. Alternating current electroluminescent devices were fabricated by first RF sputtering 30 nm-thick seed layers on top of patterned electrodes (by wet-etching of indium tin oxide-coated substrates with aqueous FeCl<sub>3</sub>/HCl or thermal evaporation of thin gold films), synthesizing nanowires to a thickness of 1.2  $\mu\text{m}$  (in the presence of 2 mM aluminium sulphate), RF sputtering of ZnS:Mn phosphor (K. J. Lesker), spin-coating of 13  $\mu\text{m}$ -thick barium titanate paste as dielectric (Dupont LuxPrint 8153), and deposition of a conductive electrode. Microfluidic devices were fabricated by standard processes, using polydimethylsiloxane (PDMS, Sylgard 184) cast off of molds composed of SU-8 photoresist (Microchem) on silicon wafers, patterned by standard lithographic techniques. The temperature within the microfluidic manifold was controlled by means of a Peltier stage. The M-I-S LED was *in situ* fabricated by sequentially synthesizing nanowires in a microfluidic manifold on top of ITO-coated glass or PET (50 °C for 30 min at flow rate = 0.6 ml h<sup>-1</sup>),

flowing in a spin-on-glass through the channel to a film thickness of 240 nm (200 °C for 10 s at flow rate = 1 ml h<sup>-1</sup>), followed by a low-melting solder that fills the remainder of the channel (In52/Sn48 from AIM Specialty) at 200 °C with low vacuum applied at the fluid outlet<sup>8</sup>. Thermodynamic calculations were performed in MATLAB. Spectroscopy and metrology were performed with the following: scanning electron microscopy (FEI XL30), atomic force microscopy (Digital Instruments Dimension 3000), transmission electron microscopy (JEOL 2010 with an EDS unit), X-ray diffractometry (PANalytical X'Pert PRO), photoluminescence (Hitachi F7000), X-ray photoelectron spectroscopy (PHI 5701 LSci), electroluminescence spectroscopy (Ocean Optics HR2000), photoluminescence spectroscopy (Nanolog fluorescence spectrometer, Horiba Jovin Yvon), luminance measurements (Konica Minolta CS-200), and solid-state device testing (custom built micromanipulator with Keithley 237 high-voltage analyzer). During scanning electron microscopy analysis, the diameter was measured at the midpoint along the *c*-axis of the nanowire.

Received 1 November 2010; accepted 9 June 2011; published online 10 July 2011

## References

- Vayssieres, L. Growth of arrayed nanorods and nanowires of ZnO from aqueous solutions. *Adv. Mater.* **15**, 464–466 (2003).
- Demianets, L. N., Kostomarov, D. V., Kuz'mina, I. P. & Pushko, S. V. Mechanism of growth of ZnO single crystals from hydrothermal alkali solutions. *Crystallogr. Rep.* **47**, S86–S98 (2002).
- Govender, K., Boyle, D. S., Kenway, P. B. & O'Brien, P. Understanding the factors that govern the deposition and morphology of thin films of ZnO from aqueous solution. *J. Mater. Chem.* **14**, 2575–2591 (2004).
- Tian, Z. R. R. *et al.* Complex and oriented ZnO nanostructures. *Nature Mater.* **2**, 821–826 (2003).

- Wagner, R. S. & Ellis, W. C. Vapor–liquid–solid mechanism of single crystal growth. *Appl. Phys. Lett.* **4**, 89–90 (1964).
- Morales, A. M. & Lieber, C. M. A laser ablation method for the synthesis of crystalline semiconductor nanowires. *Science* **279**, 208–211 (1998).
- Song, Y. J., Hormes, J. & Kumar, C. Microfluidic synthesis of nanomaterials. *Small* **4**, 698–711 (2008).
- Siegel, A. C., Bruzewicz, D. A., Weibel, D. B. & Whitesides, G. M. Microsolidics: Fabrication of three-dimensional metallic microstructures in poly(dimethylsiloxane). *Adv. Mater.* **19**, 727–733 (2007).
- Lee, S. H. *et al.* Control of the ZnO nanowires nucleation site using microfluidic channels. *J. Phys. Chem. B* **110**, 3856–3859 (2006).
- Lincot, D. Solution growth of functional zinc oxide films and nanostructures. *MRS Bull.* **35**, 778–789 (2010).
- Richardson, J. J. & Lange, F. F. Controlling low temperature aqueous synthesis of ZnO. 1. Thermodynamic analysis. *Cryst. Growth Des.* **9**, 2570–2575 (2009).
- Greene, L. E., Yuhas, B. D., Law, M., Zitoun, D. & Yang, P. D. Solution-grown zinc oxide nanowires. *Inorg. Chem.* **45**, 7535–7543 (2006).
- Ju, S. *et al.* Fabrication of fully transparent nanowire transistors for transparent and flexible electronics. *Nature Nanotech.* **2**, 378–384 (2007).
- Law, M., Greene, L. E., Johnson, J. C., Saykally, R. & Yang, P. D. Nanowire dye-sensitized solar cells. *Nature Mater.* **4**, 455–459 (2005).
- Zhang, R. & Kerr, L. L. A simple method for systematically controlling ZnO crystal size and growth orientation. *J. Solid State Chem.* **180**, 988–994 (2007).
- Demianets, L. N. & Kostomarov, D. V. Mechanism of zinc oxide single crystal growth under hydrothermal conditions. *Ann. Chim. Sci. Mater.* **26**, 193–198 (2001).
- Belghiti, H. E., Pauporté, T. & Lincot, D. Mechanistic study of ZnO nanorod array electrodeposition. *Phys. Status Solidi A* **205**, 2360–2364 (2008).
- Kisailus, D., Schwenzer, B., Gomm, J., Weaver, J. C. & Morse, D. E. Kinetically controlled catalytic formation of zinc oxide thin films at low temperature. *J. Am. Chem. Soc.* **128**, 10276–10280 (2006).
- Cha, J. N. *et al.* Silicatein filaments and subunits from a marine sponge direct the polymerization of silica and silicones *in vitro*. *Proc. Natl Acad. Sci. USA* **96**, 361–365 (1999).
- Hammond, P. T. Recent explorations in electrostatic multilayer thin film assembly. *Curr. Opin. Colloid Interface Sci.* **4**, 430–442 (1999).
- Laudise, R. A., Kolb, E. D. & Caporaso, A. J. Hydrothermal growth of large sound crystals of zinc oxide. *J. Am. Ceram. Soc.* **47**, 9–12 (1964).
- Morin, S. A., Bierman, M. J., Tong, J. & Jin, S. Mechanism and kinetics of spontaneous nanotube growth driven by screw dislocations. *Science* **328**, 476–480 (2010).
- Li, W. J., Shi, E. W., Zhong, W. Z. & Yin, Z. W. Growth mechanism and growth habit of oxide crystals. *J. Cryst. Growth* **203**, 186–196 (1999).
- Dem'yanets, L. N., Kostomarov, D. V. & Kuz'mina, I. P. Chemistry and kinetics of ZnO growth from alkaline hydrothermal solutions. *Inorg. Mater.* **38**, 124–131 (2002).
- Son, D. H., Hughes, S. M., Yin, Y. D. & Alivisatos, A. P. Cation exchange reactions in ionic nanocrystals. *Science* **306**, 1009–1012 (2004).
- Fowler, R. H. & Nordheim, L. Electron emission in intense electric fields. *Proc. R. Soc. Lond. A* **119**, 173–181 (1928).
- Jo, S. H. *et al.* Field emission of carbon nanotubes grown on carbon cloth. *J. Vac. Sci. Technol. B* **23**, 2363–2368 (2005).
- Chan, E. M., Mathies, R. A. & Alivisatos, A. P. Size-controlled growth of CdSe nanocrystals in microfluidic reactors. *Nano Lett.* **3**, 199–201 (2003).
- Wu, Y. *et al.* Inorganic semiconductor nanowires: Rational growth, assembly, and novel properties. *Chem. Eur. J.* **8**, 1260–1268 (2002).
- Wang, J. *et al.* Electrochemical fabrication of conducting polymer nanowires in an integrated microfluidic system. *Chem. Commun.* 3075–3077 (2006).

### Acknowledgements

This research was funded by the Center for Bits and Atoms (NSF CCR0122419) and the MIT Media Lab. We thank S. Manalis, V. Bulovic, and A. Belcher for generously providing use of equipment. The authors acknowledge the partial support of the Korea Foundation for Advanced Studies (awarded to J.J.) and Samsung (research internship to J.J.); the Harvard Society of Fellows (awarded to M.P.); and the Wallace H. Coulter Early Career Award, NARSAD Young Investigator Award, NSF, and NIH Director's New Innovator Award (awarded to E.S.B.).

### Author contributions

J.J. and B.Y.C. designed all the experiments. J.J. conducted all the experiments. B.Y.C. assisted with device fabrication, microfluidics, and spectroscopy. M.P. assisted with microfluidics. All authors contributed to data analysis and writing of the manuscript.

### Additional information

The authors declare no competing financial interests. Supplementary information accompanies this paper on [www.nature.com/naturematerials](http://www.nature.com/naturematerials). Reprints and permissions information is available online at <http://www.nature.com/reprints>. Correspondence and requests for materials should be addressed to J.J. or B.Y.C.